nature synthesis

Article

https://doi.org/10.1038/s44160-025-00784-w

On-surface synthesis and characterization of linear and cyclic C_6

Received: 10 October 2024

Accepted: 6 March 2025

Published online: 11 April 2025

Check for updates

Luye Sun[1,2], Yuan Guo[1,2], Wenzhi Xiang[1] & Wei Xu[1]

Cyclo[*n*]carbons, belonging to carbon clusters (C_n), have attracted substantial attention from both experimentalists and theoreticians because of their chemical structures and the controversial stabilities of their different isomers. Recently, C_{26}, C_{20}, C_{18}, C_{16}, C_{14}, C_{13}, C_{12} and C_{10} have been synthesized and characterized on thin insulating NaCl surfaces. However, synthesis of smaller cyclocarbons ($n < 10$) remains challenging due to their inherent high reactivity and increased strain. In particular, C_6 has been a subject of long-standing theoretical debate because the energy difference between its linear and cyclic forms is very small. Here we successfully generate both linear and cyclic C_6 by modulating the thickness of NaCl layers deposited on a Au(111) surface, using tip-induced dehalogenation of hexaiodobenzene (C_6I_6) molecules at 4.7 K. The linear C_6 was generated on 1-monolayer (1-ML) or 2-ML NaCl surfaces and identified as a polyynic structure through bond-resolved atomic force microscopy, verifying the theoretical calculations of a Peierls transition for linear C_6 from gas phase to on-surface adsorption. Meanwhile, cyclic C_6 could be generated on a 2-ML NaCl surface and its cumulenic nature is confirmed both experimentally and theoretically. Additionally, voltage pulses can induce cyclic C_6 to undergo either an adsorption configuration transformation from a nearly planar to a tilted geometry, or a structural transformation to the linear form.

Cyclo[*n*]carbons are molecular carbon clusters (C_n) comprising rings of *sp*-hybridized carbon atoms. Due to their high reactivity, synthesizing cyclocarbons is extremely challenging, making the chemical structures and stabilities of their different isomers a topic of substantial interest and debate[1–15]. Recently, on-surface synthesis methods have enabled the generation of cyclocarbons on thin insulating NaCl surfaces, facilitating their characterization with bond-resolved atomic force microscopy (AFM). This has led to the synthesis of various cyclocarbons, including aromatic C_{26} (ref. 16), C_{18} (refs. 17,18), C_{14} (ref. 19) and C_{10} (ref. 19), and anti-aromatic C_{20} (ref. 20), C_{16} (ref. 21), C_{13} (ref. 16) and C_{12} (ref. 20). However, their corresponding isomeric forms (for example, linear) have rarely been reported. Previous calculations have shown that when $n < 10$, the linear form of C_n is more stable than the corresponding cyclic form[22–25]; C_6 is an exception because of the very close energy difference between its linear and cyclic forms[24,26–29]. For cyclic C_6, the difficulties in synthesis and characterization become even more pronounced due to the inherent high reactivity and notable strain. Although prior gas-phase experiments have provided evidence for both C_6 isomers[30–34], their synthesis and direct real-space characterization remain exceptionally challenging.

In this work, we used scanning tunnelling microscopy (STM) tip-induced dehalogenation[35,36] to generate the linear and cyclic forms of C_6. We chose a fully halogenated benzene (hexaiodobenzene, C_6I_6) as the precursor, and through tip-induced dehalogenation, the linear C_6 form was successfully generated on the 1-monolayer (1-ML) NaCl/Au(111) surface with a yield of ~43% (164 precursors were tested; Fig. 1a). The linear C_6 form was characterized as a polyynic structure by AFM. Other observed products include linear C_6I_1 and C_6I_2 intermediates; no cyclic C_6 was obtained (Supplementary Fig. 1a–c). Interestingly, by modulating the thickness of the NaCl layers, cyclic C_6 could be

[1]Interdisciplinary Materials Research Center, School of Materials Science and Engineering, Tongji University, Shanghai, People's Republic of China. [2]These authors contributed equally: Luye Sun, Yuan Guo. e-mail: xuwei@tongji.edu.cn

https://doi.org/10.1038/s44160-025-00784-w

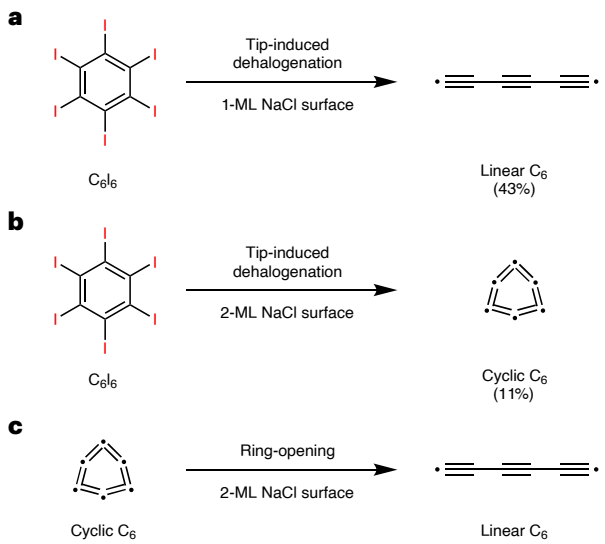

Fig. 1 | Reaction schemes for the generation of linear and cyclic C_6. a, Schematic representation of the generation of linear C_6 on a 1-ML NaCl surface. **b**, Schematic representation of the generation of cyclic C_6 on a 2-ML NaCl surface. **c**, Schematic representation of the conversion of cyclic C_6 into linear C_6 on a 2-ML NaCl surface.

generated on a 2-ML NaCl/Au(111) surface with a yield of ~11% (97 precursors were tested; Fig. 1b). Additional products include linear C_6, C_6I_1 and C_6I_2 (Supplementary Fig. 1d–g). We showed theoretically that the ring-opening barrier of cyclic C_6 is larger on the 2-ML NaCl than on the 1-ML NaCl surface. Notably, tip manipulation also allowed for the ring-opening reaction of cyclic C_6, converting it to linear C_6 (Fig. 1c).

To generate linear and cyclic C_6, C_6I_6 molecules were first introduced to a cold 1-ML NaCl/Au(111) held at ~6 K. The STM image in Fig. 2b(1) shows the C_6I_6 molecule as nearly round protrusions without discernible internal features. Subsequent high-resolution AFM imaging with a CO-terminated tip revealed the chemical structure of C_6I_6, displaying a carbon ring with six iodine atoms (Fig. 2c(1),d(1)). To trigger dehalogenation reactions, the tip was initially positioned on a single C_6I_6 molecule, and retracted by ~6–8 Å from a setpoint (typically I = 5 pA, V = 0.3 V), after that, ~3.5–4.2 V pulses were applied to the molecule with currents on the order of hundreds of fA. This procedure typically resulted in the removal of one iodine atom, forming the C_6I_5 intermediate (Fig. 2a(2)–d(2)). Subsequent voltage pulses applied to the C_6I_5 intermediates led to the formation of C_6I_4 and C_6I_3 intermediates, as shown in the STM and AFM images (Fig. 2a(3)–d(3),a(4)–d(4)).

Further application of voltage pulses induced additional dehalogenation of the intermediates (C_6I_4, C_6I_3), resulting in linear intermediates and the final linear C_6 product. The STM image (Fig. 2b(5)) displays a dumbbell shape with two bright protrusions at the ends. AFM imaging clearly reveals its chemical structure, identifying it as the linear C_6I_2 intermediate, where three triple bonds and two iodine atoms are distinctly resolved (Fig. 2c(5),d(5)). Additional voltage pulses targeting the C–I bonds sequentially removed the iodine atoms, leading to the formation of the linear C_6I_1 intermediate (Fig. 2b(6)–d(6)) and ultimately the final product, linear C_6 (Fig. 2b(7)–d(7)). The AFM images unambiguously reveal three triple bonds of linear C_6, confirming its polyynic structure on the NaCl surface.

Previous theoretical studies have predicted that the linear C_6 form adopts a cumulenic structure as the lowest-energy geometry in the gas phase[24,26,28] (see also the bond length calculations in Fig. 3b at the ωB97XD/def2-TZVP level). However, interestingly, when relaxing the cumulenic C_6 on the NaCl surface with the experimentally determined registry, a polyynic structure of C_6 with alternating bond lengths was obtained as shown in Fig. 3b, indicating a Peierls transition occurred within linear C_6 from gas phase to on-surface adsorption. From the relaxed structural model of linear C_6 (Fig. 3e,f), an arch-shaped geometry is seen with the central triple bond elevated, which aligns with the AFM observations (Fig. 3c,d). This configuration is hypothesized to arise from the strong interactions between the carbon radicals at both termini and the NaCl substrate.

The strong interaction between the linear C_6 form and the NaCl substrate, which hinders the diffusion of C_6 on the surface, makes it possible to successfully measure the electronic states of this small molecular carbon structure (Fig. 3g). The dI/dV spectra, represented by the black and red lines in Fig. 3g, were acquired for the triple and single bonds of linear C_6, respectively. The spectrum recorded for the triple bond shows a prominent peak at approximately V = −1.5 V, with no other obvious states observed. Similarly, the single-bond spectrum also displays a prominent peak at around V = −1.5 V, and an additional rising state starting from V = 1.5 V is observed. STM images obtained at these bias voltages correspond to positive ion resonance (PIR) and negative ion resonance (NIR) (Fig. 3h,i). The PIR/NIR images acquired using a metallic tip and a CO tip show consistent characteristics (Supplementary Fig. 2). Further STM simulations of the highest occupied molecular orbital and the lowest unoccupied molecular orbital are in good agreement with the experimental STM images. Notably, the simulated STM image at a lower positive bias compared to the lowest unoccupied molecular orbital also exhibits similar features (Supplementary Fig. 3).

To generate cyclic C_6, we then attempted to achieve tip-induced dehalogenation of C_6I_6 molecules on a 2-ML NaCl/Au(111) surface. The STM and AFM images we obtained (Fig. 4b(1)–d(1)) confirm the structure of the C_6I_6 molecule, consistent with the results obtained on the 1-ML NaCl surface. Applying several voltage pulses (~3.5–4.2 V pulses with the tip retracting by ~6–8 Å from a setpoint I = 0.5 pA, V = 0.3 V with currents on the order of hundreds of fA) to C_6I_6 molecules led to the formation of typical intermediates (for example, C_6I_5, C_6I_4, C_6I_3), as shown in the STM and AFM images (Fig. 4b(2)–d(2),b(3)–d(3),b(4)–d(4)). Notably, various C_6I_4 and C_6I_3 intermediates generated on the 1-ML NaCl were also observed on the 2-ML NaCl surface. Further voltage pulses induced additional dehalogenation of these intermediates, leading to the formation of C_6I_2 and C_6I_1 intermediates (Fig. 4b(5)–d(5),b(6)–d(6)). Linear C_6I_2 and C_6I_1 were also observed on the 2-ML NaCl during manipulation (Supplementary Fig. 1).

Finally, further voltage pulses led to complete dehalogenation and the formation of a round protrusion in the STM image (Fig. 4b(7)). Based on previous theories[8,11,12,24,26,28], cyclic C_6 is predicted to be a D_{3h} cumulenic structure, based on this being the lowest-energy geometry, and to feature a relatively large bond-angle alternation (BAA = 59.1°) (see the calculations of cyclic C_6 in the gas phase in Supplementary Fig. 4). High-resolution AFM imaging (Fig. 4c(7),d(7)) clearly shows a triangular carbon ring with no halogen atoms attached, which can be unambiguously recognized as a cyclic C_6 structure. In addition, cyclic C_6 represents a uniform feature in AFM images (see also Supplementary Figs. 5 and 6), which naturally indicates a cumulenic structure, in a good agreement with theoretical calculations (BLA = 0°) of cyclic C_6 both in the gas phase and on the NaCl surface (Fig. 4e). It is noticeable that cyclic C_6 possesses a comparatively large BAA of 59.1° (Supplementary Fig. 4) compared with already-generated even-number cyclocarbons on the surface (for example, BAA_{C10} = 41.5°, BAA_{C12} = 36.9°, BAA_{C14} = 25.3°, $BAA_{C16} \approx 0$, $BAA_{C18} \approx 0$, $BAA_{C20} \approx 0$, $BAA_{C26} \approx 0$)[11], which is a consequence of its smaller size. Our calculations demonstrate that the cyclic C_6 is more prone to undergoing ring-opening reactions on the 1-ML NaCl surface (energy barrier, 1.56 eV) than on the 2-ML NaCl surface (energy barrier, 2.32 eV), aligning well with the experimental observations that generation of cyclic C_6 is achieved on the 2-ML surface via tip manipulation (Supplementary Figs. 7 and 8). Interestingly, we observed that cyclic C_6 can also

https://doi.org/10.1038/s44160-025-00784-w

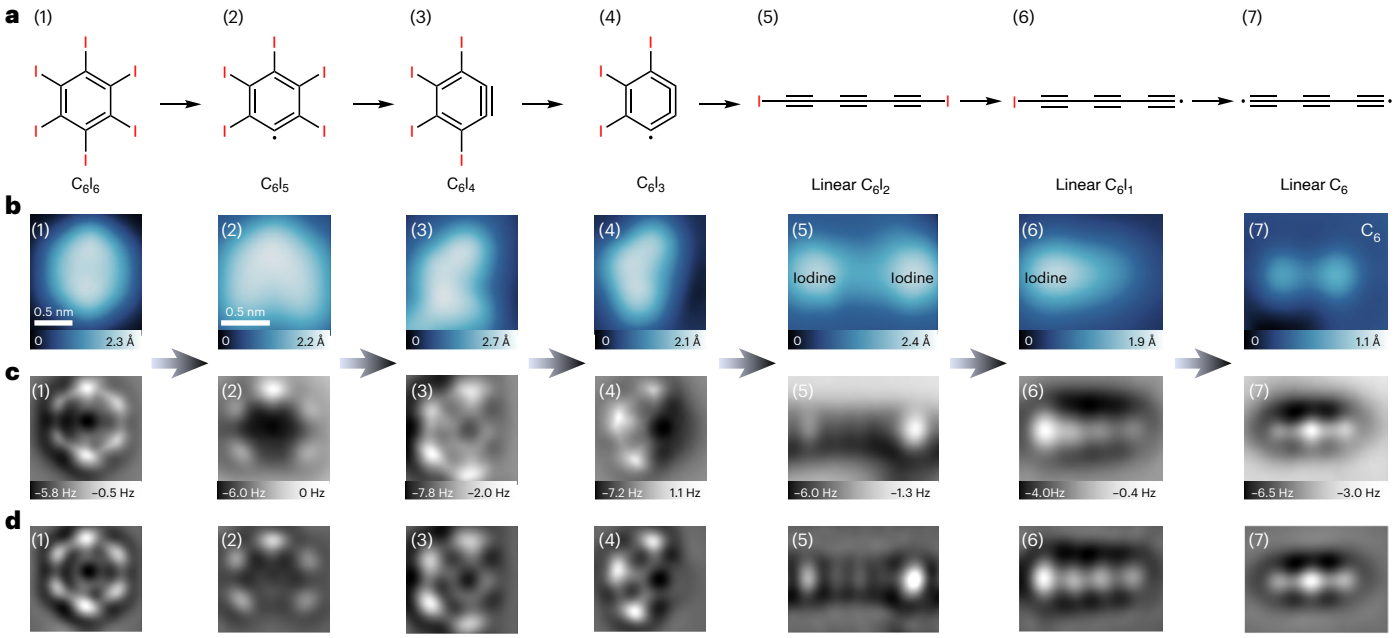

Fig. 2 | On-surface-generated precursor, intermediates and product (linear C_6) on a 1-ML NaCl surface. a–d, Molecules (**a**), STM images (**b**), AFM images (**c**) and Laplace-filtered AFM images (**d**) of precursor, intermediates and product. The scale bar in **b(1)** applies to all experimental and Laplace-filtered images of the precursor; the scale bar in **b(2)** applies to all experimental and Laplace-filtered images of intermediates and product. STM setpoints: $I = 1$ pA, $V = 0.3$ V for **b(1)**, $I = 5$ pA, $V = 0.3$ V for **b(2)**–**b(7)**. AFM tip offsets Δz: −0.6 Å, +0.5 Å, −0.3 Å, −0.4 Å, +0.2 Å, +0 Å, −0.8 Å for **c(1)**–**c(7)**, respectively. Reference setpoints of Δz: $I = 1$ pA, $V = 0.3$ V for **c(1)**, $I = 5$ pA, $V = 0.3$ V for **c(2)**–**c(7)**.

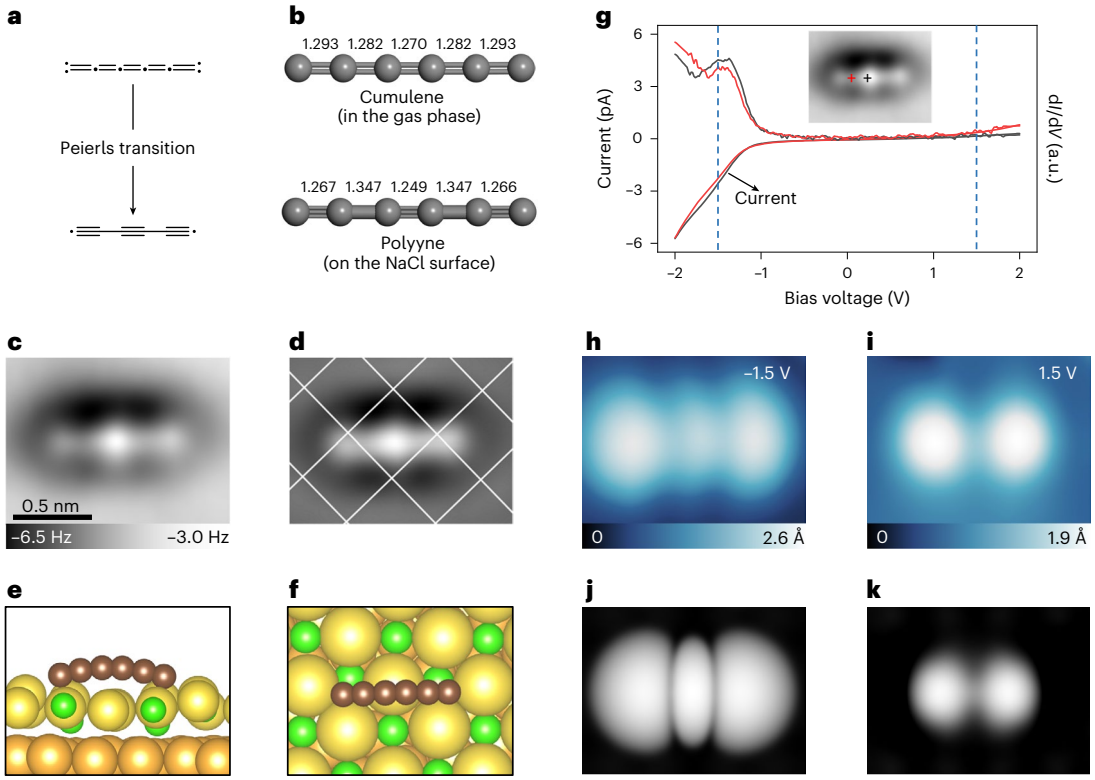

Fig. 3 | Characterization of linear C_6. a,b, Schematic representation of Peierls transition of linear C_6 from gas phase to on-surface adsorption (**a**) with calculated bond lengths (Å) (**b**). **c,d**, AFM (**c**) and Laplace-filtered AFM (**d**) images of linear C_6. Crossings of white lines mark the chloride ion positions of the NaCl surface determined experimentally. **e,f**, Side (**e**) and top (**f**) views of the calculated structure of linear C_6 on the NaCl surface. **g**, Scanning tunnelling spectroscopy of linear C_6 on NaCl. The differential conductance (dI/dV) spectra were measured for the triple bond (black line) and the single bond (red line) of linear C_6, respectively, as marked by black and red crosses. **h,i**, STM images of linear C_6 acquired with the same CO-terminated tip: PIR (**h**); NIR (**i**). STM setpoints: $I = 5$ pA, $V = -1.5$ V (**h**); $I = 5$ pA, $V = 1.5$ V (**i**). **j,k**, Simulated STM images of linear C_6 on the NaCl surface, showing the calculated highest occupied molecular orbital (**j**) and the lowest unoccupied molecular orbital (**k**). The scale bar in **c** applies to all experimental and simulated STM images. AFM tip offset Δz: −0.8 Å for **c**. Reference setpoint of Δz: $I = 5$ pA, $V = 0.3$ V.

https://doi.org/10.1038/s44160-025-00784-w

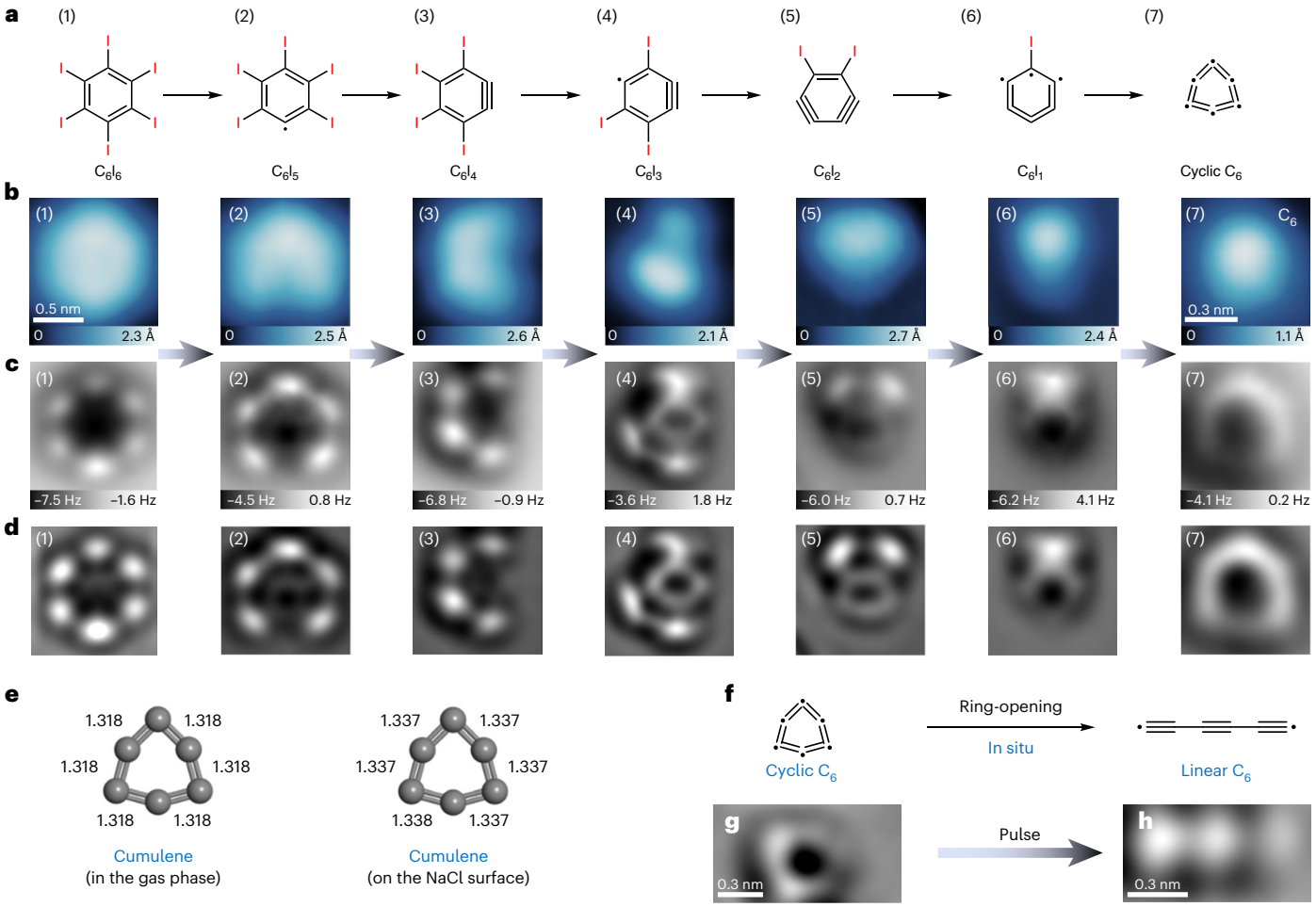

Fig. 4 | On-surface-generated precursor, intermediates and product (cyclic C_6) on a 2-ML NaCl surface. a–d, Molecules (**a**), STM images (**b**), AFM images (**c**) and Laplace-filtered AFM images (**d**) of the precursor, intermediates and product (cyclic C_6). The scale bar in **b(1)** applies to all experimental and Laplace-filtered images of the precursor and intermediates; the scale bar in **b(7)** applies to all experimental and Laplace-filtered images of the product. **e**, Bond length (Å) calculations of cyclic C_6 in the gas phase and on the NaCl surface. **f**, In situ transformation of cyclic C_6 to linear C_6 via tip-induced ring-opening reaction. **g**,**h**, Corresponding Laplace-filtered AFM images of cyclic C_6 (**g**) and linear C_6 (**h**). STM setpoints: $I = 0.5$ pA, $V = 0.3$ V for **b(1)**–**b(7)**. AFM tip offsets Δz: +1.5 Å, +0.8 Å, +0.4 Å, +1.5 Å, +0.7 Å, +0.5 Å, +0 Å for **c(1)**–**c(7)**, respectively. Reference setpoints of Δz: $I = 0.8$ pA, $V = 0.3$ V for **c(1)**,**c(3)**; $I = 2$ pA, $V = 0.3$ V for **c(4)**; $I = 0.5$ pA, $V = 0.3$ V for **c(2)**,**c(5)**–**c(7)**.

undergo an in situ transformation into linear C_6 via a ring-opening reaction by a voltage pulse, in which three triple bonds are clearly resolved within linear C_6 (Fig. 4f–h). A classical single-molecule retro-Bergman reaction product is shown in Supplementary Fig. 9.

In addition to the ring-opening reaction of cyclic C_6, we also observed that a smaller bias voltage (-3 V) could induce cyclic C_6 to adopt different adsorption configurations on the NaCl surface. AFM images (Fig. 5a(1),(2)) reveal a near-planar adsorption configuration of cyclic C_6 with a triangular shape, corresponding well with the density functional theory (DFT)-calculated structure (Fig. 5a(3),(4)) based on the experimentally determined adsorption site (Fig. 5a(2)). After applying a voltage pulse (-3 V), cyclic C_6 diffuses several nanometres across the NaCl surface, and notably, subsequent AFM images (Fig. 5b(1),(2)) identify that the triangular-shaped cyclic C_6 has transformed into a bright protrusion, ~80 pm higher than the near-planar configuration. DFT calculations based on the experimental adsorption site (Fig. 5b(3),(4)) indicate that the cyclic C_6 adopts a more tilted adsorption configuration, ~79 pm higher than the planar configuration shown in Fig. 5a(4). This tilted configuration of cyclic C_6 can be converted back to the near-planar state through further tip manipulation, demonstrating the reversibility of the configuration transformations (Fig. 5c(1)–(4)). Due to the high mobility of cyclic C_6 on the NaCl surface, the electronic states were challenging to probe (Supplementary Figs. 10 and 11).

In conclusion, we have successfully generated linear and cyclic C_6 forms on the NaCl surfaces by atom manipulation at 4.7 K. Bond-resolved AFM imaging confirmed the polyynic and cumulenic structures of linear C_6 and cyclic C_6, consistent with theoretical calculations. Additionally, the frontier molecular orbitals of linear C_6 were probed through scanning tunnelling spectroscopy. By applying voltage pulses, cyclic C_6 can either undergo a structural transformation into linear C_6 or alter its adsorption configuration from a near-planar to a tilted form. This study offers an approach for the generation of small carbon clusters by modulating the thickness of NaCl layers, which may be extended to a more general molecular carbon system.

Methods

Experimental details for STM and AFM measurements

STM and AFM measurements were carried out in a commercial (Createc) low-temperature system operated at 4.7 K with a base pressure better than 1×10^{-10} mbar. The single-crystalline Au(111) surface was cleaned by several sputtering and annealing cycles. The NaCl films were obtained by thermally evaporating NaCl crystals onto a clean Au(111) surface at room temperature, resulting in islands of 1-ML and 2-ML

https://doi.org/10.1038/s44160-025-00784-w

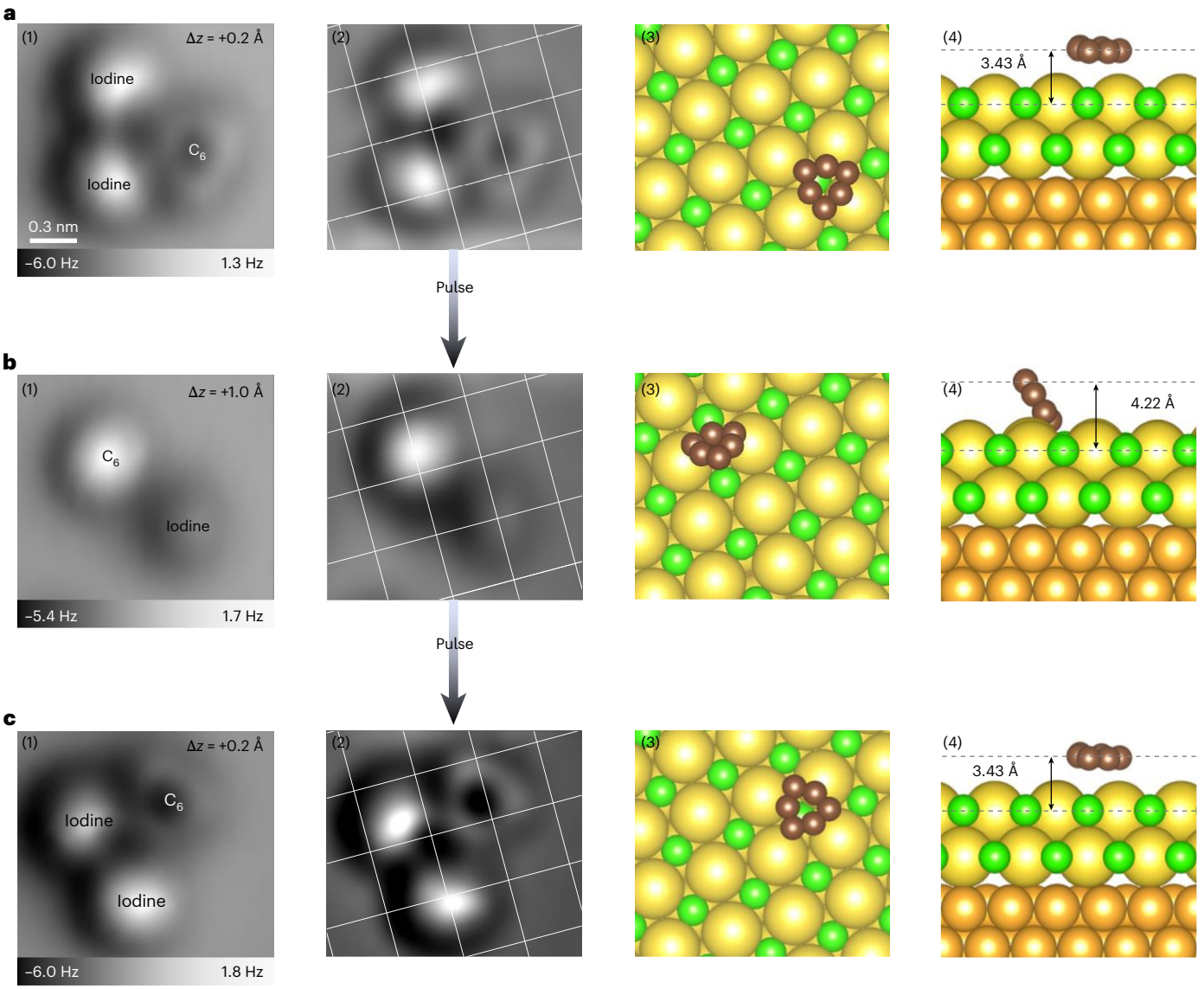

Fig. 5 | Tip-induced adsorption configuration transformations of cyclic C_6. **a**–**c**, AFM images (**a(1)**–**c(1)**) and Laplace-filtered AFM images (**b(2)**–**c(2)**) of a cyclic C_6 with different adsorption configurations during tip manipulation, and corresponding top views (**a(3)**–**c(3)**) and side views (**a(4)**–**c(4)**) of DFT-relaxed cyclic C_6 on the NaCl surface. All the AFM images (**a(1)**–**c(1)**) were acquired with the same CO tip. Crossings of white lines (**a(2)**–**c(2)**) mark chloride ion positions on the NaCl surface determined experimentally. The scale bar in **a(1)** applies to all experimental images. Reference setpoints of Δ*z*: *I* = 0.6 pA, *V* = 0.3 V for (**a(1)**–**c(1)**).

thickness. Hexaiodobenzene (C_6I_6, purchased from Sigma-Aldrich) molecules were deposited on a cold NaCl/Au(111) surface by thermal sublimation. CO molecules for tip modification[37] were dosed onto the cold sample via a leak valve. We used qPlus sensors[38] with a resonance frequency f_0 = 29.49 kHz, quality factor $Q \approx 45{,}000$ and a spring constant $k \approx 1{,}800$ N m^{-1}, operating in frequency-modulation mode[39]. The bias voltage V was applied to the sample with respect to the tip. AFM images were acquired in constant-height mode at V = 0 V and an oscillation amplitude of A = 1 Å. The tip-height offsets Δz for constant-height AFM images are defined as the offset in tip–sample distance relative to the STM setpoint at the NaCl surface. The positive (negative) values of Δz correspond to the tip–sample distance increased (decreased) with respect to a STM setpoint. More details about reaction routes for the formation of linear and cyclic C_6 are shown in Supplementary Figs. 12 and 13.

DFT calculations

DFT calculations were carried out in the gas phase using the Gaussian 16 program package[40]. ωB97XD exchange-correlation functional[41] in conjunction with def2-TZVP[42] basis sets was used for the linear and cyclic C_6 calculations in the gas phase.

The Vienna Ab initio Simulation Package (VASP)[43,44] was used to perform the DFT calculations on the NaCl surface. Interactions between electrons and ions were described using the projector-augmented wave method[45,46]. The Perdew–Burke–Ernzerhof generalized gradient approximation exchange-correlation functional[47] was employed. Van der Waals corrections to the Perdew–Burke–Ernzerhof density functional were also included using the DFT-D3 method of Grimme et al.[48]. The kinetic energy cut-off was set to 400 eV. We used a 1-ML or 2-ML NaCl(001) slab on top of Au(111) substrate modelled by a three-layer slab; the bottom layer of the Au(111) was fixed. Atomic structures were relaxed until the atomic forces were <0.03 eV Å^{-1}. Transition states were found by the climbing image nudged elastic band[49] and dimer methods[50], and all local minima and saddle points were optimized until the forces on all unconstrained atoms were ≤0.03 eV Å^{-1}. Simulated STM images were obtained based on the Tersoff–Hamann method[51,52].

Data availability

All data are available in the main text or the Supplementary Information.

References

1. Parent, D. C. & McElvany, S. W. Investigations of small carbon cluster-ion structures by reactions with hydrogen cyanide. *J. Am. Chem. Soc.* **111**, 2393–2401 (1989).
2. Van Orden, A. & Saykally, R. J. Small carbon clusters: spectroscopy, structure, and energetics. *Chem. Rev.* **98**, 2313–2357 (1998).
3. Grutter, M. et al. Electronic absorption spectra of linear C_6, C_8 and cyclic C_{10}, C_{12} in neon matrices. *J. Chem. Phys.* **111**, 7397–7401 (1999).
4. Diederich, F. Carbon scaffolding: building acetylenic all-carbon and carbon-rich compounds. *Nature* **369**, 199–207 (1994).
5. Pitzer, K. S. & Clementi, E. Large molecules in carbon vapor. *J. Am. Chem. Soc.* **81**, 4477–4485 (1959).
6. Parasuk, V., Almlof, J. & Feyereisen, M. W. The [18] all-carbon molecule: cumulene or polyacetylene? *J. Am. Chem. Soc.* **113**, 1049–1050 (1991).
7. Torelli, T. & Mitas, L. Electron correlation in C_{4N+2} carbon rings: aromatic versus dimerized structures. *Phys. Rev. Lett.* **85**, 1702–1705 (2000).
8. Arulmozhiraja, S. & Ohno, T. CCSD calculations on C_{14}, C_{18}, and C_{22} carbon clusters. *J. Chem. Phys.* **128**, 114301 (2008).
9. Remya, K. & Suresh, C. H. Carbon rings: a DFT study on geometry, aromaticity, intermolecular carbon–carbon interactions and stability. *RSC Adv.* **6**, 44261–44271 (2016).
10. Baryshnikov, G. V., Valiev, R. R., Kuklin, A. V., Sundholm, D. & Ågren, H. Cyclo[18]carbon: insight into electronic structure, aromaticity, and surface coupling. *J. Phys. Chem. Lett.* **10**, 6701–6705 (2019).
11. Baryshnikov, G. V. et al. Aromaticity of even-number cyclo[*n*] carbons (*n*=6–100). *J. Phys. Chem. A* **124**, 10849–10855 (2020).
12. Charistos, N. D. & Muñoz-Castro, A. Induced magnetic field in *sp*-hybridized carbon rings: analysis of double aromaticity and antiaromaticity in cyclo[2*N*]carbon allotropes. *Phys. Chem. Chem. Phys.* **22**, 9240–9249 (2020).
13. Baryshnikov, G. V. et al. Odd-number cyclo[*n*]carbons sustaining alternating aromaticity. *J. Phys. Chem. A* **126**, 2445–2452 (2022).
14. Brémond, E., Pérez-Jiménez, A. J., Adamo, C. & Sancho-García, J. C. Stability of the polyynic form of C_{18}, C_{22}, C_{26}, and C_{30} nanorings: a challenge tackled by range-separated double-hybrid density functionals. *Phys. Chem. Chem. Phys.* **24**, 4515–4525 (2022).
15. Li, M. et al. Potential molecular semiconductor devices: cyclo-C_n (*n*=10 and 14) with higher stabilities and aromaticities than acknowledged cyclo-C_{18}. *Phys. Chem. Chem. Phys.* **22**, 4823–4831 (2020).
16. Albrecht, F. et al. The odd-number cyclo[13]carbon and its dimer, cyclo[26]carbon. *Science* **384**, 677–682 (2024).
17. Kaiser, K. et al. An *sp*-hybridized molecular carbon allotrope, cyclo[18]carbon. *Science* **365**, 1299–1301 (2019).
18. Scriven, L. M. et al. Synthesis of cyclo[18]carbon via debromination of $C_{18}Br_6$. *J. Am. Chem. Soc.* **142**, 12921–12924 (2020).
19. Sun, L. et al. On-surface synthesis of aromatic cyclo[10]carbon and cyclo[14]carbon. *Nature* **623**, 972–976 (2023).
20. Sun, L. et al. On-surface synthesis and characterization of anti-aromatic cyclo[12]carbon and cyclo[20]carbon. *Nat. Commun.* **15**, 7649 (2024).
21. Gao, Y. et al. On-surface synthesis of a doubly anti-aromatic carbon allotrope. *Nature* **623**, 977–981 (2023).
22. Hoffmann, R. Extended Hückel theory—V: cumulenes, polyenes, polyacetylenes and C_n. *Tetrahedron* **22**, 521–538 (1966).
23. Liang, C. & Schaefer, H. F. III Carbon clusters: the structure of C_{10} studied with configuration interaction methods. *J. Chem. Phys.* **93**, 8844–8849 (1990).
24. Hutter, J., Lüthi, H. P. & Diederich, F. Structures and vibrational frequencies of the carbon molecules C_2–C_{18} calculated by density functional theory. *J. Am. Chem. Soc.* **116**, 750–756 (1994).
25. Watts, J. D. & Bartlett, R. J. The nature of monocyclic C_{10}. A theoretical investigation using coupled-cluster methods. *Chem. Phys. Lett.* **190**, 19–24 (1992).
26. Martin, J. M. L. & Taylor, P. R. Structure and vibrations of small carbon clusters from coupled-cluster calculations. *J. Phys. Chem.* **100**, 6047–6056 (1996).
27. Yen, T. W. & Lai, S. K. Use of density functional theory method to calculate structures of neutral carbon clusters C_n ($3 \le n \le 24$) and study their variability of structural forms. *J. Chem. Phys.* **142**, 084313 (2015).
28. Brito, B. G. A., Hai, G. Q. & Cândido, L. Quantum Monte Carlo study on the structures and energetics of cyclic and linear carbon clusters C_n (*n*=1,..., 10). *Phys. Rev. A* **98**, 062508 (2018).
29. Parasuk, V. & Almlöf, J. The electronic and molecular structure of C_6: complete active space self-consistent-field and multireference configuration interaction. *J. Chem. Phys.* **91**, 1137–1141 (1989).
30. Yang, S. et al. UPS of 2–30-atom carbon clusters: chains and rings. *Chem. Phys. Lett.* **144**, 431–436 (1988).
31. Szczepanski, J. & Vala, M. Correlation of infrared and UV–visible bands of matrix-isolated carbon clusters. *J. Phys. Chem.* **95**, 2792–2798 (1991).
32. Presilla-Márquez, J. D., Sheehy, J. A., Mills, J. D., Carrick, P. G. & Larson, C. W. Vibrational spectra of cyclic C_6 in solid argon. *Chem. Phys. Lett.* **274**, 439–444 (1997).
33. Wang, S. L., Rittby, C. M. L. & Graham, W. R. M. Detection of cyclic carbon clusters. I. Isotopic study of the $\nu_4(e')$ mode of cyclic C_6 in solid Ar. *J. Chem. Phys.* **107**, 6032–6037 (1997).
34. Fulara, J., Riaplov, E., Batalov, A., Shnitko, I. & Maier, J. P. Electronic and infrared absorption spectra of linear and cyclic C_6^+ in a neon matrix. *J. Chem. Phys.* **120**, 7520–7525 (2004).
35. Pavliček, N. et al. On-surface generation and imaging of arynes by atomic force microscopy. *Nat. Chem.* **7**, 623–628 (2015).
36. Pavliček, N. et al. Polyyne formation via skeletal rearrangement induced by atomic manipulation. *Nat. Chem.* **10**, 853–858 (2018).
37. Gross, L., Mohn, F., Moll, N., Liljeroth, P. & Meyer, G. The chemical structure of a molecule resolved by atomic force microscopy. *Science* **325**, 1110–1114 (2009).
38. Giessibl, F. J. High-speed force sensor for force microscopy and profilometry utilizing a quartz tuning fork. *Appl. Phys. Lett.* **73**, 3956–3958 (1998).
39. Albrecht, T. R., Grütter, P., Horne, D. & Rugar, D. Frequency modulation detection using high-*Q* cantilevers for enhanced force microscope sensitivity. *J. Appl. Phys.* **69**, 668–673 (1991).
40. Frisch, M. J. et al. Gaussian 16 rev. C.01 (Gaussian, 2016).
41. Chai, J. D. & Head-Gordon, M. Long-range corrected hybrid density functionals with damped atom-atom dispersion corrections. *Phys. Chem. Chem. Phys.* **10**, 6615–6620 (2008).
42. Weigend, F. & Ahlrichs, R. Balanced basis sets of split valence, triple zeta valence and quadruple zeta valence quality for H to Rn: design and assessment of accuracy. *Phys. Chem. Chem. Phys.* **7**, 3297–3305 (2005).
43. Kresse, G. & Hafner, J. Ab initio molecular dynamics for open-shell transition metals. *Phys. Rev. B* **48**, 13115–13118 (1993).
44. Kresse, G. & Furthmüller, J. Efficient iterative schemes for ab initio total-energy calculations using a plane-wave basis set. *Phys. Rev. B* **54**, 11169–11186 (1996).
45. Blöchl, P. E. Projector augmented-wave method. *Phys. Rev. B* **50**, 17953–17979 (1994).
46. Kresse, G. & Joubert, D. From ultrasoft pseudopotentials to the projector augmented-wave method. *Phys. Rev. B* **59**, 1758–1775 (1999).

47. Perdew, J. P., Burke, K. & Ernzerhof, M. Generalized gradient approximation made simple. *Phys. Rev. Lett.* **77**, 3865–3868 (1996).
48. Grimme, S., Antony, J., Ehrlich, S. & Krieg, H. A consistent and accurate ab initio parametrization of density functional dispersion correction (DFT-D) for the 94 elements H–Pu. *J. Chem. Phys.* **132**, 154104 (2010).
49. Henkelman, G., Uberuaga, B. P. & Jonsson, H. A climbing image nudged elastic band method for finding saddle points and minimum energy paths. *J. Chem. Phys.* **113**, 9901–9904 (2000).
50. Kästner, J. & Sherwood, P. Superlinearly converging dimer method for transition state search. *J. Chem. Phys.* **128**, 014106 (2008).
51. Vanpoucke, D. E. P. & Brocks, G. Formation of Pt-induced Ge atomic nanowires on Pt/Ge(001): a density functional theory study. *Phys. Rev. B* **77**, 241308 (2008).
52. Tersoff, J. & Hamann, D. R. Theory of the scanning tunneling microscope. *Phys. Rev. B* **31**, 805–813 (1985).

Acknowledgements

The authors acknowledge financial support from the National Key R&D Program of China (2023YFE0101900), the Ministry of Science and Technology of the People's Republic of China, the National Natural Science Foundation of China (22125203, 22402149) and the Shanghai Science and Technology Program (24ZR1470000).

Author contributions

W. Xu conceived the research. L.S., Y.G. and W. Xiang performed the STM/AFM experiments. L.S. and Y.G. carried out the DFT calculations. All authors contributed to writing the manuscript.

Competing interests

The authors declare no competing interests.

Additional information

Supplementary information The online version contains supplementary material available at https://doi.org/10.1038/s44160-025-00784-w.

Correspondence and requests for materials should be addressed to Wei Xu.

Peer review information *Nature Synthesis* thanks Pascal Ruffieux and the other, anonymous, reviewer(s) for their contribution to the peer review of this work. Primary Handling Editor: Peter Seavill, in collaboration with the *Nature Synthesis* team.